Computational Thermal Sciences, 2(5):xxx–xxx, 2010

THERMAL RECEPTIVITY OF FREE CONVECTIVE FLOW FROM A HEATED VERTICAL SURFACE: NONLINEAR WAVES

Manosh C. Paul,[1,*] D. Andrew S. Rees,[2] & Michael Wilson[2]

[1] *Department of Mechanical Engineering, University of Glasgow, Glasgow G12 8QQ, UK*

[2] *Department of Mechanical Engineering, University of Bath, Bath BA2 7AY, UK*

[*] Address all correspondence to Manosh C. Paul E-mail: m.paul@mech.gla.ac.uk

In a previous paper (Int. J. Thermal. Sci., vol. **47***, pp. 1382–1392, 2008), the authors performed a detailed numerical investigation of the linear instability of the thermal boundary layer flow over a vertical surface by introducing unsteady thermal disturbances near the leading edge and by solving numerically the fully elliptic linearized stability equations. The main aim of the present paper is to extend those results into the nonlinear regime by seeding the boundary layer with similar disturbances of finite amplitude. The ensuing nonlinear waves are found to exhibit a variety of behaviours, depending on the precise amplitude and period of the forcing. When the amplitude is sufficiently small, the linearized theory of the previous work is reproduced, but for larger amplitudes, cell splitting or cell merging may occur as waves travel downstream. Cell splitting takes place when disturbance frequencies are somewhat smaller than the most strongly amplified nondimensional disturbance frequency of* 0.4 *for which the boundary layer response, is at its greatest in terms of the surface rate of heat transfer (see Fig. 8 in previous paper). Cell merging takes place at frequencies what are approximately double that of the most strongly amplified disturbance frequency. Attention is focussed on fluids with a unit Prandtl number.*

KEY WORDS: *nonlinear instability, thermal receptivity, free convection, boundary layer*

1. INTRODUCTION

The effect of introducing a time-periodic thermal disturbance near the leading edge of a vertical thermal boundary layer was considered in Paul et al. (2008). Such disturbances are analogous to the spatially localized disturbances introduced within the boundary layer by the presence of suction/blowing slots [e.g., see Fasel and Konzelmann (1990), or the varying thermal source of Brooker et al. (1997) and Herwig and You (1997)]. When such thermal forcing is of sufficiently small magnitude, a relatively large transient response travels downstream leaving behind a time–periodic state. Convection cells are found to stretch gradually as they travel downstream due to the fact that the basic boundary layer accelerates. The local amplitude of the periodic response follows what is expected from linear stability theory using the parallel flow assumption, namely, that it decays or grows spatially in a manner that is roughly in accord with the predicted growth rates for a constant frequency [see Fig. 11 of Paul et al. (2008)].

In the context of free convection, there are a moderate number of papers that deal with free convection within either square or rectangular containers with sidewall heating and cooling, and that therefore have a close relationship to the present external flow. Examples of these studies are the papers by Janssen and Armfield (1996) and Armfield and Patterson (1991) and an entire issue of the *International Journal for Numerical Methods in Fluids* (vol. **40**, no. 8, pp. 951–1144, 2002), which is devoted to the types of numerical method used for modeling convection in an 8×1 cavity. However, there is a substantial difference between these cavity flows and the flow considered here; within cavities the wave disturbances leave the ascending hot boundary layer, travel across the top of the cavity, and seed disturbances into the descending cold

1940–2503/10/$35.00

NOMENCLATURE

a	scaling factor
A	amplitude of the thermal disturbance
C	function of ξ and η
d	parameter to control A
J	Jacobian
M	maximum local response
N	minimum local response
Pr	Prandtl number
$q_{\rm loc}$	surface rate of heat transfer, Eq. (11)
t	time
x, y	nondimensional Cartesian coordinates

Greek Symbols

λ	temporal frequency
θ	nondimensional temperature
ϕ	angle from the vertical
ψ	streamfunction
ω	vorticity
ξ, η	similarity variables

Subscripts

max	maximum value
min	minimum value

Superscripts

$\bar{}$	steady flow quantities
$\hat{}$	disturbance quantities

boundary layer. In turn, this introduces disturbances back into the base of the hot boundary layer. Thus, a feedback mechanism is set up that does not have a counterpart here. Moreover, when the hot and cold boundary layers in a cavity are distinct, the core region is thermally stratified, unlike the present situation where the ambient temperature outside the boundary layer is uniformly cold.

To date, there appears to be no published paper dealing with nonlinear phenomena in the vertical boundary layer treated as an external flow except for the early experimental study of Szewczyk (1962) who used a dye-injection technique to follow the transition to turbulence in water. In that very early paper, there appears to be no systematic approach to determining criteria for the onset of secondary instabilities, which take the form of pairs of counter-rotating streamwise vortices. In the present paper, we choose to concentrate on a simpler problem, namely, the response of the boundary layer to time-periodic two-dimensional thermal disturbances placed on the surface near the leading edge. The aim of the present paper, then, is to extend the analysis of Paul et al. (2008) into the nonlinear regime, and our objective is to determine the different ways in which nonlinear effects are manifested when the boundary layer is subjected to such time-periodic disturbances.

2. NONLINEAR DISTURBANCE EQUATIONS

The full nonlinear equations of motion were presented in Paul et al. (2008), and their derivation is omitted for the sake of brevity; they take the form,

$$\frac{\partial^2\hat{\psi}}{\partial\xi^2}+\frac{\partial^2\hat{\psi}}{\partial\eta^2}=C\hat{\omega}, \tag{1}$$

$$C\frac{\partial\hat{\omega}}{\partial t}=\frac{\partial^2\hat{\omega}}{\partial\xi^2}+\frac{\partial^2\hat{\omega}}{\partial\eta^2}+J(\bar{\psi},\hat{\omega})+J(\hat{\psi},\bar{\omega})+J(\hat{\psi},\hat{\omega}) + C^{1/2}\left(\frac{\partial\hat{\theta}}{\partial\xi}\sin\frac{\phi}{4}+\frac{\partial\hat{\theta}}{\partial\eta}\cos\frac{\phi}{4}\right), \tag{2}$$

$$C\frac{\partial\hat{\theta}}{\partial t}=\frac{1}{\rm Pr}\left(\frac{\partial^2\hat{\theta}}{\partial\xi^2}+\frac{\partial^2\hat{\theta}}{\partial\eta^2}\right)+J(\bar{\psi},\hat{\theta})+J(\hat{\psi},\bar{\theta})+J(\hat{\psi},\hat{\theta}), \tag{3}$$

where C, ξ, and η are defined according to

$$C(\xi,\eta)=\left(\frac{3}{4}\right)^{2/3}\left(\xi^2+\eta^2\right)^{1/3}$$
$$\left[\frac{3}{4}\left(\xi+i\eta\right)\right]^4=\left(x+iy\right)^3, \tag{4}$$

the Jacobian operator, J, is defined according to

$$J(\psi,\chi)=\frac{\partial\psi}{\partial\xi}\frac{\partial\chi}{\partial\eta}-\frac{\partial\psi}{\partial\eta}\frac{\partial\chi}{\partial\xi}, \tag{5}$$

(where χ represents either the temperature or the vorticity) and where overbars and circumflexes denote the steady basic flow variables and the disturbance quantities, respectively. In the above equations, the value, ϕ, is the angular coordinate measured from the upward vertical; it is not possible to give a simple closed-form expression for this in terms of ξ and η, but it is straightforward to

produce the exact values numerically. The boundary conditions to solve the above system of equations are

$$\hat{\psi} = \hat{\psi}_\eta = 0, \quad \hat{\theta} = 0 \quad \text{on} \quad \eta = \eta_{\min} = 0, \quad (6)$$

$$\hat{\psi} = \hat{\psi}_\xi = 0, \quad \hat{\theta}_\xi = 0 \quad \text{on} \quad \xi = \xi_{\min}, \quad (7)$$

$$\hat{\psi}_\eta = 0, \quad \hat{\omega} = 0, \quad \hat{\theta} = 0 \quad \text{as} \quad \eta = \eta_{\max}, \quad (8)$$

and a buffer/sponge region is used near to the outflow boundary, $\xi = \xi_{\max}$, in order to dampen out disturbances and prevent the growth of unphysical reflections; full details of our procedure may also be found in Paul et al. (2008).

The steady state basic flow is computed first, as described in detail in Paul et al. (2008). Then the nonlinear disturbance Eqs. (1)–(3) are solved for a variety of disturbance frequencies and amplitudes in order to determine the nonlinear characteristics of the disturbed boundary layer flow. The instabilities are induced in the same way as in Paul et al. (2008), namely, by introducing the following time-periodic thermal disturbance on the heated surface near the leading edge:

$$\hat{\theta}(\xi, 0) = Ae^{-a(\xi-\xi_0)^2} \sin(\lambda t), \quad (9)$$

where λ is the temporal frequency, $a = 0.1$ a chosen scaling factor, A the disturbance amplitude, and where $\xi_0 = 20$ defines the location of the leading edge of the heated surface. As nonlinear waves are being considered, the magnitude of A is now important. In fact, when A is sufficiently large (e.g., $A = 2 \times 10^{-5}$ when $\lambda = 0.4$) the starting transient is sufficiently powerful that regions of high shear and high temperature gradient are formed. The very poor resolution associated with these regions causes the numerical method to become highly inaccurate and sometimes unstable. Therefore, we adopted an ad hoc procedure whereby A is regarded as a function of t, which rises slowly from 10^{-8} (a level for which no numerical instability arises for any value of λ) to the required amplitude. Therefore, the negative effects of a large starting transient are reduced substantially and the flow is able to settle to a time-periodic state. We used the following expression for $A(t)$:

$$\log_{10}[A(t)] = -8 + d(1 - e^{-bt})^2. \quad (10)$$

This expression shows that $A = 10^{-8}$ initially, but $A \to 10^{-8+d}$ as $t \to \infty$. The value $b = 0.01$ was found to yield suitably good results when 15,000 time steps of length $\delta t = 0.1$ were taken. Once the transients have decayed, the resulting time-periodic response of the boundary layer was found to be independent of the value of b that was chosen.

Much of our description of the dynamics of the instability involves the rate of heat transfer at the surface, and therefore, it is convenient to define the quantity,

$$q_{\text{loc}}(\xi, t) = -\left.\frac{\partial \hat{\theta}}{\partial \eta}\right|_{\eta=0}. \quad (11)$$

Of course, this expression yields different values when compared with the y derivative, but given that we are generally interested either in where $q_{\text{loc}} = 0$, or in variations in time at a fixed point in space, the distinction between the different derivatives is not important.

3. NUMERICAL METHOD

Finite difference techniques were used to solve the system of nonlinear Eqs. (1)–(3). The two equations with time derivatives were discretized using second-order accurate central difference approximations, and the DuFort-Frankel scheme was employed for the time derivative. The Jacobian terms were approximated using the Arakawa (1966) formulation, which was designed to be particularly suitable for unsteady flows. Neumann boundary conditions were approximated using a standard ghost point approach, which therefore maintains second-order accuracy and has an asymptotically smaller discretization error than a one-sided first-order approximation.

The Poisson equation (1) was solved using a multigrid correction scheme algorithm to accelerate iterative convergence. It incorporates a V-cycle algorithm involving line Gauss-Seidel relaxation. The method is based on the pointwise method described in Briggs (1987), but it adopts two line relaxations per coordinate direction on each multigrid level.

In the simulation, $\xi_{\max} = 620$ was chosen as the location of the outflow boundary and the buffer region started from $\xi = 520$. The buffer domain technique of the outflow boundary follows the methodology introduced by Kloker et al. (1993).

A total of 480 steps were used in the range ξ direction with a uniform step length, $\delta\xi = 1.25$. In the η direction, 48 equal intervals were used in the $0 \le \eta \le \eta_{\max} = 12$, and therefore the step length was $\delta\eta = 0.25$. Given that the step lengths satisfy $\delta\xi = 5\delta\eta$, which corresponds to a cell aspect ratio of 5, a line relaxation method is essential to maintain a fast iterative convergence of the Poisson equation, even with multigrid smoothing. We were able

to take five multigrid levels, and each V-cycle was comprised of two relaxation sweeps in each coordinate direction for each grid. At each time step, the new vorticity and temperature fields are calculated first, followed by the solution of the Poisson equation for the streamfunction, and finally the boundary vorticity is computed in the way presented in Roache (1972).

Finally, it is essential to undertake grid independence tests to check the values of δt, $\delta\xi$, and $\delta\eta$ used in the simulations. These were undertaken by halving the intervals in both directions. Details may be found in the Appendix.

4. COMPUTATIONS FOR $\lambda = 0.4$

In this section, we consider the forcing frequency, $\lambda = 0.4$, because the linear analysis of Paul et al. (2008) shows that the this frequency elicits the largest response of the boundary layer to periodic forcing; therefore, we call this the most strongly amplified disturbance frequency for the linear regime. We have found that the maximum value of A for which we were able to compute solutions is $A = 2 \times 10^{-5}$. At larger values of A, the strength of the nonlinearity is such that the generation of narrow shear layers causes numerical instability due to poor spatial resolution, as mentioned above. Therefore, we concentrate on this maximum value of A, and various views of the resulting flow are given in Figs. 1–4.

Figure 1 shows how the time variation of $q_{\rm loc}$ varies with distance along the boundary layer. Because the magnitude of the heat transfer may vary over many orders of magnitude as ξ increases, each curve in Fig. 1 has been normalized to display the same amount of vertical variation, and the mean value of each curve is located at the corresponding value of ξ on the ordinate of the graph; this convention also applies to other figures of the same type. The accelerating nature of the basic boundary layer may be seen in Fig. 1 by tracking the spatial location of, say, the maximum value of $q_{\rm loc}$ as t increases.

For small values of ξ, the variation in the surface heat transfer is sinusoidal and the boundary layer response is still within the linear regime. However, strong wave steepening occurs at larger values of ξ, which indicates the presence of nonlinearity. At such distances from the leading edge (e.g., $\xi = 520$ or, equivalently, $x = 2850$), the value of $q_{\rm loc}$ is seen to decrease very slowly and then to rise sharply before the next gentle decrease. The sharp rise is associated with the streamwise advection of the region near the heated surface just upstream of where the isotherms displayed in Figs. 2 and 3 are widely spaced (e.g., see the black triangle in Fig. 3). In Figs. 2 and 3,

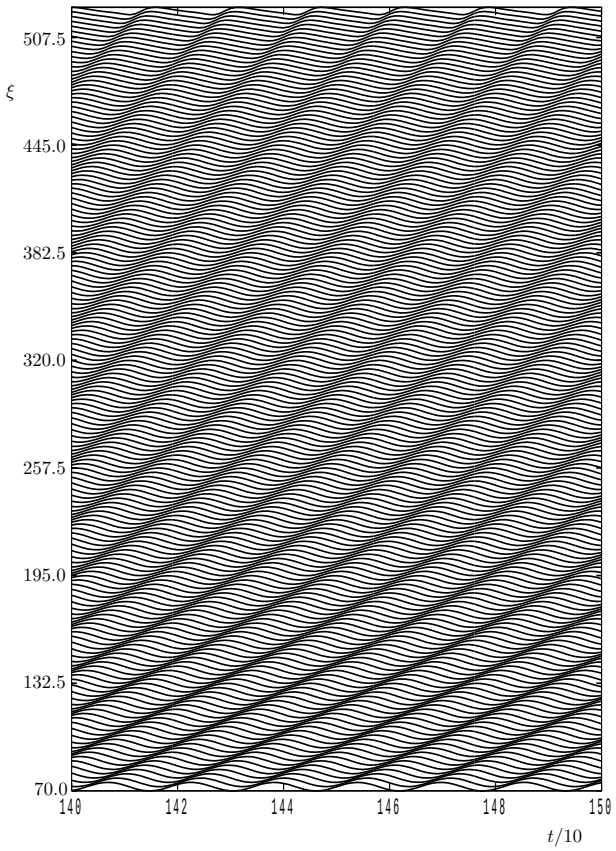

FIG. 1: Variation with t of the normalised values of $q_{\rm loc}$. The forcing frequency and amplitude are $\lambda = 0.4$ and $A = 2 \times 10^{-5}$, respectively.

we also see how the evolving wave like disturbances have become sufficiently strong that a severe distortion of the overall thermal field is obtained. When A is chosen to take larger values, then similar distortions occur progressively further upstream.

Figure 4 shows contours of $q_{\rm loc}$ as a function of both x and t. Of particular interest here is how the symmetry between positive and negative rates of heat transfer is broken as the flow becomes nonlinear. At the large values of x, the "nose" corresponding to $q_{\rm loc} = 8 \times 10^{-2}$ (e.g., at $x = 2700$ and $t = 1410$) occurs at a smaller value of x than does that corresponding to $q_{\rm loc} = -8 \times 10^{-2}$ (e.g., at $x = 2740$ and $t = 1406$). This lack of symmetry is caused by an essential difference in the thermal response to a strong flow directed toward the surface and one away from it. In the former case, cold fluid is pushed toward the surface causing a large positive change in the rate of heat transfer. In the latter case, the hot fluid is pulled away

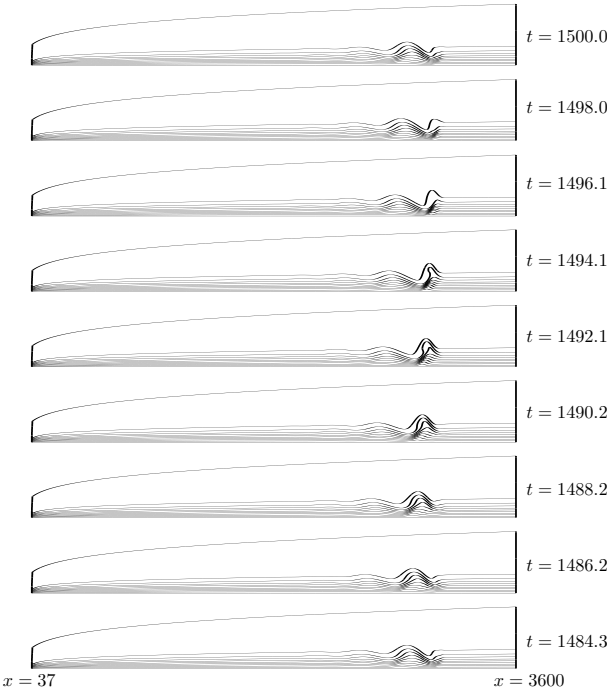

FIG. 2: Isotherms of the θ field at eight equally spaced time intervals over one forcing period for $\lambda = 0.4$ and $A = 2 \times 10^{-5}$. Contours are drawn at intervals of 0.1.

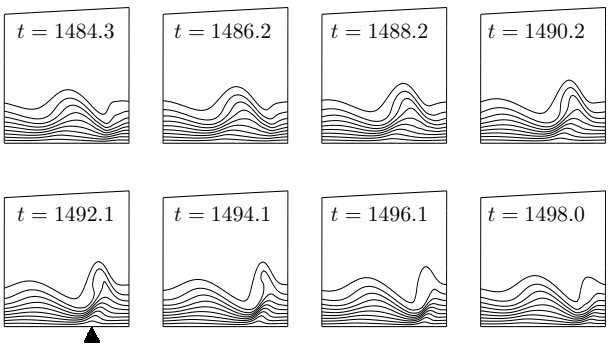

FIG. 3: Close-up view of the isotherms (θ) shown in Fig. 2. Each frame is plotted in the range $2500 < x < 3080$. The black triangle indicates where $q_{\rm loc}$ attains its minimum value.

from the surface, but because the overall temperature gradient cannot become positive (since that would imply the existence of a region of fluid that is hotter than the surface). The value of $q_{\rm loc}$ must therefore be bounded below, but it is effectively unbounded above.

Qualitatively similar results to those shown above are obtained when λ takes values fairly close to 0.4, although

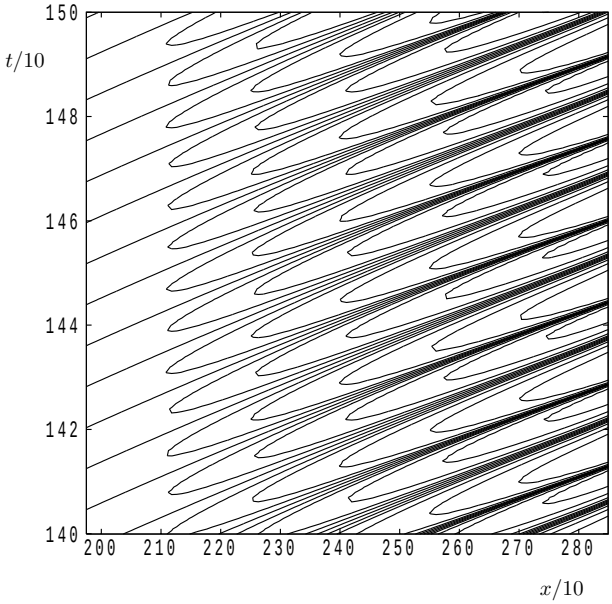

FIG. 4: Contours of $q_{\rm loc}$ $\lambda = 0.4$, and $A = 2 \times 10^{-5}$. The contour levels are at $\pm 8 \times 10^{-2}$, $\pm 4 \times 10^{-2}$, $\pm 2 \times 10^{-2}$, $\pm 10^{-2}$, $\pm 5 \times 10^{-3}$, and 0. The contours, $q_{\rm loc} = 0$, are those that cross the ordinate.

it is possible to use larger values of A in these cases since the spatial growth of the disturbance is smaller as λ recedes from 0.4. However, when λ differs substantially from 0.4, new nonlinear effects arise and these form the subject of the next few sections and is the primary focus of this paper.

5. SUPERHARMONIC RESONANCES $(\lambda < 0.4)$

In this section, we will cover those cases for which the forcing frequency is < 0.4. When λ is sufficiently small, the presence of nonlinearities serves to substantially modify the manner in which waves travel downstream, and the patterns obtained are entirely different from those given by the linearized theory presented in Paul et al. (2008). That this should happen is easily understood if, when considering the evolution with ξ of a disturbance with $\lambda = 0.2$, it is realized that the nonlinear interaction of the corresponding wave train with itself generates waves with double the local wavenumber. Such waves are then of roughly the same wavelength as those generated by a disturbance with frequency $\lambda = 0.4$, and they are therefore able to grow preferentially. This could be termed a 1:2 superharmonic resonance because the local wavenumber is found to double at a position in the boundary layer,

which turns out to be dependent on both the amplitude and frequency of the initiating disturbance.

Other superharmonic resonances, namely, 1:3 and 1:4, occur as λ decreases, and these are also shown below. Further resonances of this type are suspected to be likely to occur, but the present computational domain is insufficiently large to represent them well.

5.1 1:2 Superharmonic Resonance

The nonlinear evolution of the flow for values of λ close to 0.2 are considered. The manner in which the flow develops is again depicted in a variety of ways in order to gain some understanding of the role played by the amplitude and frequency of the disturbance. Some examples of this development are shown in Figs. 5–9.

Figure 5 shows how the evolution of $q_{\rm loc}$ with time changes its character as ξ increases for the case, $\lambda = 0.18$, when the disturbance amplitude is $A = 2 \times 10^{-3}$. Figure 5 shows clearly that the boundary layer responds at the same frequency as the thermal forcing when $\xi \in (70, 300)$, but that it responds at twice the frequency when

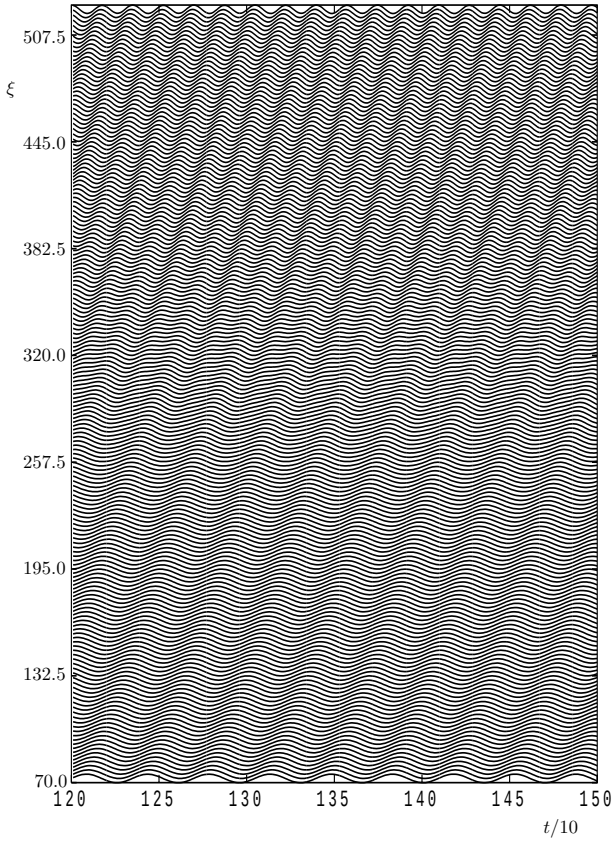

FIG. 5: Variation with t of $q_{\rm loc}$ for the 1:2 superharmonic resonance, where $\lambda = 0.18$ and $A = 2 \times 10^{-3}$.

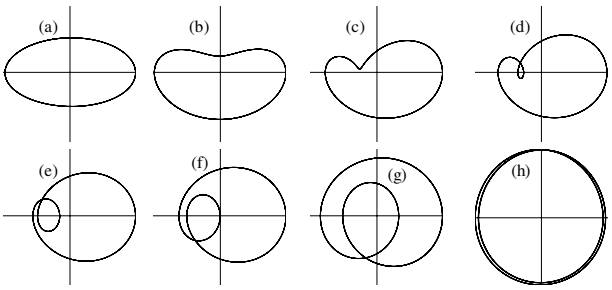

FIG. 6: Limit cycles of the phase trajectories of $q_{\rm loc}$ at various positions along the surface for $\lambda = 0.18$, $A = 2 \times 10^{-3}$: (a) $\xi = 175$, (b) $\xi = 270$, (c) $\xi = 288$, (d) $\xi = 300$, (e) $\xi = 313$, (f) $\xi = 325$, (g) $\xi = 350$, and (h) $\xi = 500$. The horizontal coordinate is $q_{\rm loc}$, while the vertical coordinate is $\partial q_{\rm loc}/\partial t$.

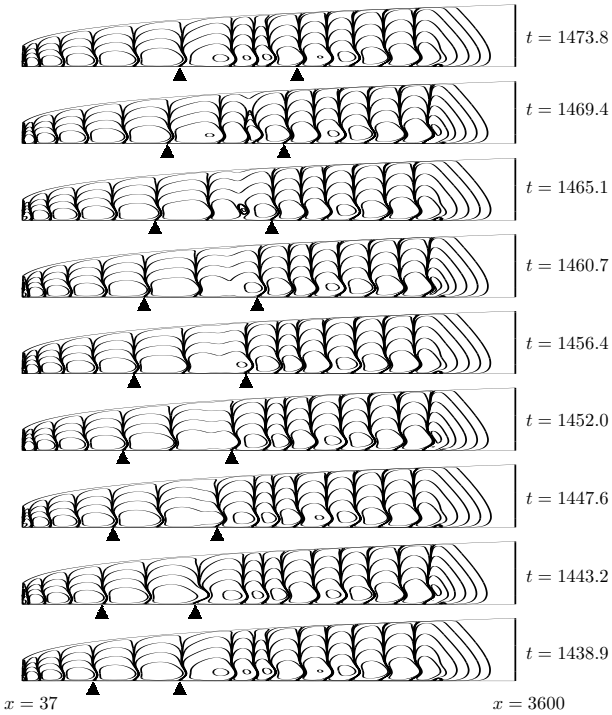

FIG. 7: Isotherms of $\hat{\theta}$ at eight equally spaced times in one period for $\lambda = 0.18$ and $A = 2 \times 10^{-3}$. Contours are plotted for $\hat{\theta} = \pm$ (10^{-2}, 10^{-3}, 10^{-4}, 10^{-5}, 10^{-6}, and 10^{-7}). The black triangles mark the start and end of a complete cell pair at $t = 1438.9$, which becomes two pairs at $t = 1473.8$, one forcing period later.

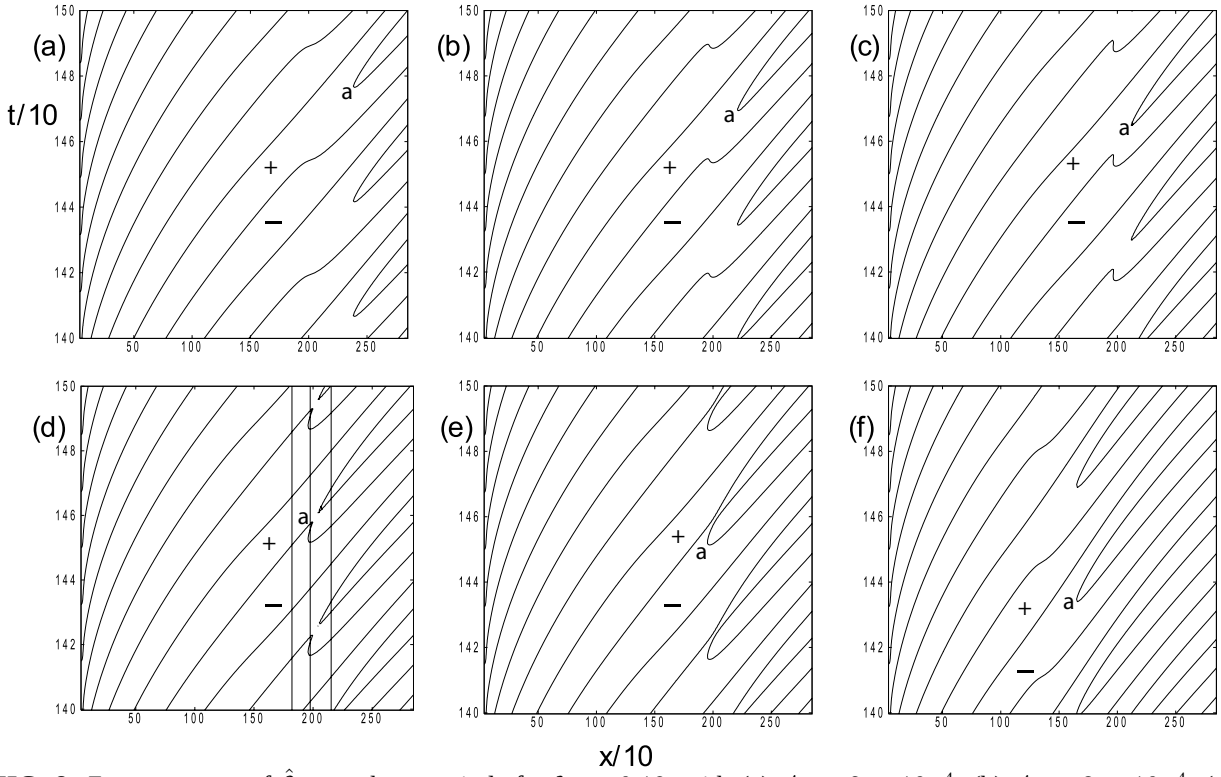

FIG. 8: Zero contours of $\hat{\theta}$ over three periods for $\lambda = 0.18$, with (a) $A = 2 \times 10^{-4}$, (b) $A = 3 \times 10^{-4}$, (c) $A = 3.5 \times 10^{-4}$, (d) $A = 3.8 \times 10^{-4}$, (e) $A = 4 \times 10^{-4}$, and (f) $A = 2 \times 10^{-3}$. Positive $(+)$ and negative $(-)$ signs correspond to where $q_{\rm loc} > 0$ and < 0, respectively.

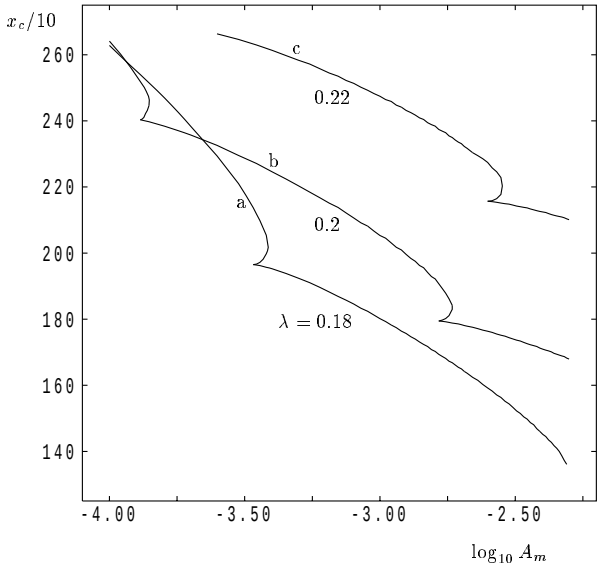

FIG. 9: Variation with A of the position of the 1:2 superharmonic resonance for (a) $\lambda = 0.18$, (b) $\lambda = 0.2$, and (c) $\lambda = 0.22$.

$\xi > 350$, with a short transition regime between the two regions. The temporal frequency within the second region is 0.36, which is close to the most strongly amplified disturbance frequency, 0.4. At the maximum value of ξ depicted in Fig. 5, the variation with time of the heat transfer is roughly sinusoidal, showing that the disturbances to the basic flow are still too small to have yet reached the fully nonlinear regime. However, the 1:2 resonance is a nonlinear phenomenon and it may be explained by the very different spatial growth rates associated with the $\lambda = 0.18$ and the $\lambda = 0.36$ wave trains. The former grows slowly relative to the latter, and the self-interaction of the former causes a disturbance of the form of the latter which then grows more rapidly and eventually dominates after a certain distance has been traveled.

In Fig. 6, we show the limit cycles of the phase trajectories of $q_{\rm loc}$ at different positions along the surface. In Fig. 6, as with others of its type presented later, the horizontal coordinate is $q_{\rm loc}$, while the vertical coordinate is $\partial q_{\rm loc}/\partial t$, which was calculated using a central difference approximation in time.

Figure 6a is close to being an ellipse, which indicates that the waves are roughly sinusoidal and confirms the above statement that the disturbance is still essentially linear. As ξ increases, the flow becomes progressively contaminated by the growing superharmonic wave. At a point just downstream of $\xi = 288$ and upstream of $\xi = 300$ (Figs. 6c and 6d, respectively) a loop develops in the phase trajectory and it is this position which may be considered to mark the transition point between the two regimes. At $\xi = 500$ (Fig. 6i), the second loop is almost identical to the first loop and this represents the full establishment of the superharmonic response. Again, these final loops are roughly circular, which confirms the linearity of the disturbance.

We emphasise that the transition from Figs. 6a–6h is not a period doubling, because the curves are drawn over only one forcing period. Rather, this represents a period halving and is one that occurs spatially, rather than temporally or as a governing parameter changes.

In Fig. 7, we have plotted a corresponding set of disturbance isotherms over eight equally spaced intervals over a complete forcing period in time. The maximum and minimum levels shown are $\pm 10^{-2}$, and therefore, the magnitude of the disturbance field is not particularly large. The black triangles shown in Fig. 7 represent one wavelength corresponding to the thermal forcing frequency and are used to show the manner in which the period halving takes place. As t increases, the leading cell of the two elongates, compared to the second, and eventually splits into three by the generation of a small cell of the opposite sign; this is a typical scenario for other values of A and λ.

Contours corresponding to $q_{\rm loc} = 0$ over three forcing periods have been plotted in Fig. 8 in order to aid the investigation of the effect of different disturbance amplitudes on the qualitative nature of the resonance. Here, the forcing frequency remains at $\lambda = 0.18$, but A takes different values. In Fig. 8, thermal cells are delineated by the contours and the number of cells that exist at a chosen value of x may be determined by placing a vertical line at that value of x and counting the intervals between the intersections of the line with the contours. Figure 8d shows an example with three vertical lines placed near the transition region. At the left hand line, 6 cells (3 pairs) exist, but these undergo a complex transformation to 12 cells (6 pairs) at the right hand line. The middle line shows the manner in which the new cells appear. The positions marked by "a" in Fig. 8 correspond to the appearance or disappearance of cells. In Figs. 8a, 8b, 8e, and 8f, a new cell simply appears in the middle of an already-established but distended cell. In the other images, the resonance process is more complicated; a careful inspection of Fig. 8d shows that one cell transforms to three, then a different grouping of three becomes one by destroying the middle cell, and then a final one-to-three transformation takes place. Thus, when A is relatively small a cell for which $q_{\rm loc} > 0$ splits into three, but when A is relatively large, this happens to a cell for which $q_{\rm loc} < 0$.

It is clear from Fig. 8 that the position at which the appearance of new cells occur depends on the forcing amplitude, A. Figure 8 also suggests that cell splitting occurs nearer to the leading edge as A increases, which is intuitive. This has been investigated using many more values of A than are represented in Fig. 8 and for the three values, $\lambda = 0.18, 0.2$, and 0.22; the results are shown in Fig. 9.

The curves shown in Fig. 9 correspond to where cells are either created or destroyed, or in mathematical terms, where the contours $q_{\rm loc} = 0$ in Fig. 8 have turning points; we denote these positions by x_c. Figure 9 clearly shows the general trend for x_c to increase as the forcing amplitude decreases, although the evolution of x_c with A is not straightforward. On taking the $\lambda = 0.18$ curve, it is seen that there are three values at $\log_{10} A = -3.4$ (i.e., $A \approx 3.8 \times 10^{-4}$), which correspond to the three turning points displayed in Fig. 8d. Given that resonance begins at the smallest value of x_c for an given value of A, it is clear that as A decreases the value of x_c increases to ~ 1960, after which it jumps to near 2130, which is near where a is placed in Fig. 8d. Similar jumps occur at the other values of λ. We also see the general trend for x_c to increase as λ increases (at least over the range of values presented).

5.2 1:3 Superharmonic Resonance

In this section, we present the nonlinear evolution of the flow for forcing frequencies which are close to $\lambda = (1/3) \times 0.4$. In this case, the nonlinear self-interaction of the wave train should generate new waves with three times the wavenumber obtained by linear theory. This development is displayed in Figs. 10–13 in an identical fashion to those for 1:2 superharmonic case.

Figure 10 shows the variation of $q_{\rm loc}$ for the case where $\lambda = 0.13$ and the disturbance amplitude is $A = 4 \times 10^{-2}$ [i.e., $d \simeq 6.60$ in Eq. (10)]. Figure 10 clearly shows that there are now three different spatial wavelengths present in three different regions, which are given approximately by $\xi \in (70, 190)$, $\xi \in (190, 320)$, and $\xi \in (320, 520)$.

The first region, $\xi \in (70, 190)$, is where the waves oscillate with the forcing frequency $\lambda = 0.13$ and these are again generated directly by the thermal forcing. At the end of the first region, there is a transition to a regime that

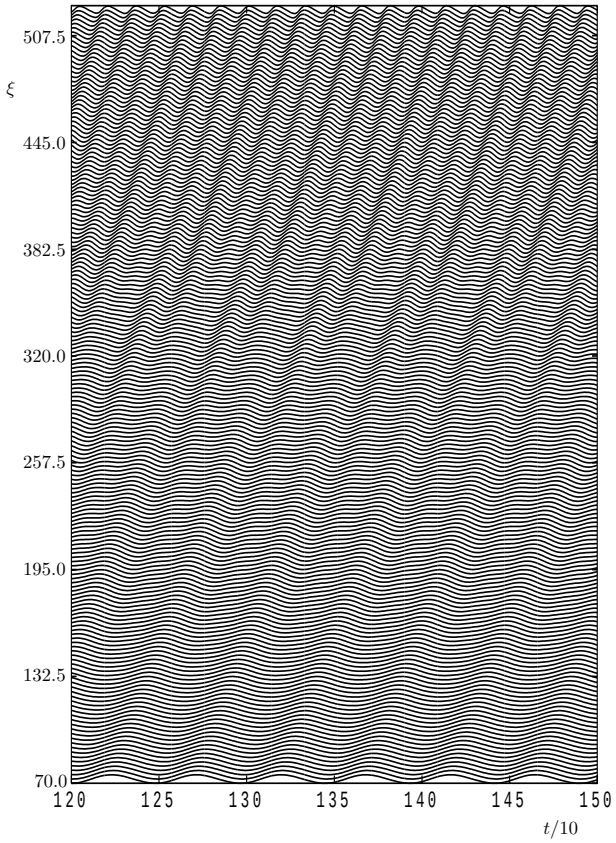

FIG. 10: Variation with t of the normalised values of $q_{\rm loc}$ for the 1:3 superharmonic resonance in the case where $\lambda = 0.13$ and $A = 4 \times 10^{-2}$.

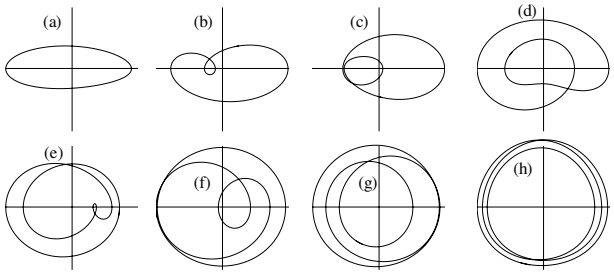

FIG. 11: Limit cycles of the phase trajectories of $q_{\rm loc}$ at various positions along the surface for $\lambda = 0.13$, and $A = 4 \times 10^{-2}$: (a) $\xi = 75$, (b) $\xi = 225$, (c) $\xi = 275$, (d) $\xi = 313$, (e) $\xi = 338$, (f) $\xi = 363$, (g) $\xi = 400$, and (h) $\xi = 450$. The horizontal coordinate is $q_{\rm loc}$, while the vertical coordinate is $\partial q_{\rm loc}/\partial t$.

oscillates with double the original frequency. The temporal frequency within this second region, i.e., at $\xi \in (190, 320)$ is 0.26; this transition is quite similar to that

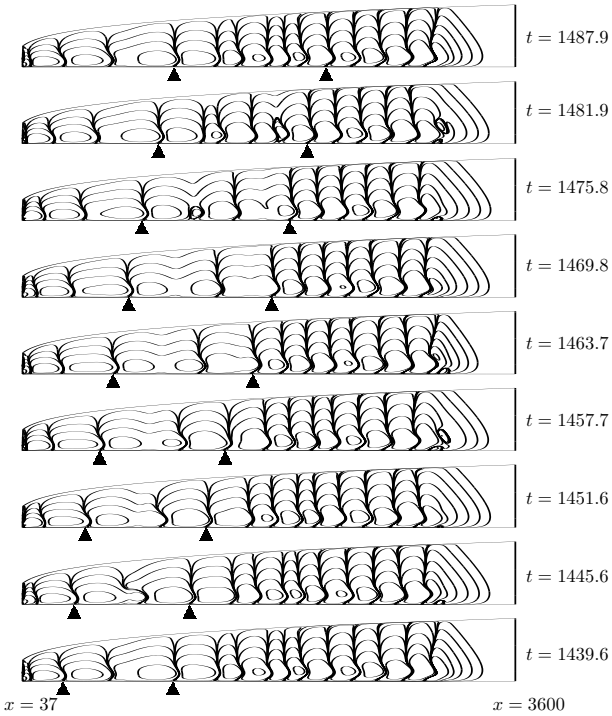

FIG. 12: Contours of disturbance temperature ($\hat{\theta}$) at eight equally spaced intervals in a forcing period for $\lambda = 0.13$ and $A = 4 \times 10^{-2}$. The contour levels are $\hat{\theta} = \pm\,(10^{-1}, 10^{-2}, 10^{-3}, 10^{-4}, 10^{-5}, 10^{-6})$. The black triangles mark the start and end of a complete cell pair at $t = 1439.6$, which becomes three pairs at $t = 1487.9$.

seen in Fig. 5 for the 1:2 superharmonic resonance case. At the end of the second region, there is a second transition to a state where the waves oscillate with three times the original frequency. Within this third region, the temporal frequency is 0.39, which is very close to the most strongly amplified disturbance frequency. We note that a similar sequence of transitions involving the spatial evolution of vortices in a free convective boundary layer in porous media is given in Rees (2003). In that work, a spatially evolving steady vortex system first doubles the number of vortices per unit spanwise length and then affects a second smooth transition to three times the original number of vortices.

Figure 11 shows the limit cycles of the phase trajectories of $q_{\rm loc}$ at various distances from the leading edge. Figure 11a is close to being an ellipse, indicating again that the waves are essentially linear. As ξ increases, the disturbance becomes progressively contaminated by the growing superharmonic waves. The first transition occurs between Figs. 11a and 11b. Two well-established loops

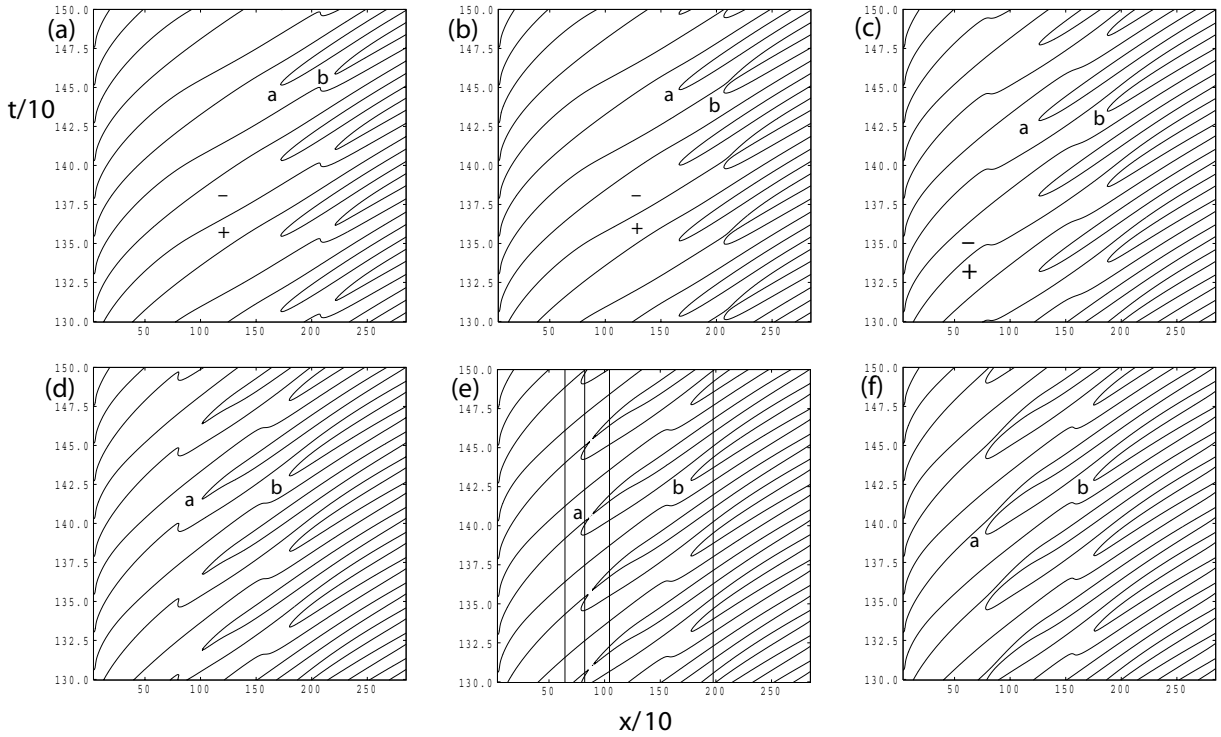

FIG. 13: Zero contours of $q_{\rm loc}$ over the last few periods in time for $\lambda = 0.13$, where (a) $A = 1.4 \times 10^{-2}$, (b) $A = 1.6 \times 10^{-2}$, (c) $A = 4 \times 10^{-2}$, (d) $A = 5.2 \times 10^{-2}$, (e) $A = 5.6 \times 10^{-2}$, and (f) $A = 6 \times 10^{-2}$.

appear at $\xi = 313$ (Fig. 11d), but these are of very different amplitudes. This may be seen clearly near $\xi = 320$ in Fig. 10, where the wave train has alternating maxima. The second transition occurs just upstream of $\xi = 338$ (Fig. 11e). At $\xi = 450$ (Fig. 11h), the three loops are almost identical and roughly elliptical.

Figure 12 shows the corresponding set of disturbance isotherms over eight equal intervals during one forcing period. The successive contours in Fig. 12 correspond to negative integer powers of 10 multiplied by the maximum absolute value of the isotherm field, which is $\sim 10^{-1}$. The pairs of black triangles included in Fig. 12 again represent one wavelength corresponding to the thermal forcing frequency. As t increases, the trailing cell between the triangles at first elongates, compared to the second, and then splits into three with the generation of a new small cell. In a similar manner, when $t > 1463.7$, the leading cell of the original pair elongates, splits, and generates a new cell, finally becoming three.

Contours of $q_{\rm loc}$ over the last few periods are shown in Fig. 13. A variety of forcing amplitudes are represented for $\lambda = 0.13$. Once more, it is shown clearly that the manner in which the superharmonic resonance takes place is highly dependent on the forcing amplitude. For small values of A (e.g., $A = 1.4 \times 10^{-2}$ and Fig. 13a), regions within which $q_{\rm loc} < 0$ each spawn two internal regions with positive rates of heat transfer; whereas for the 1:2 superharmonic case, it was only one region that was spawned. Thus, one cell splits into five. On the other hand, in Figs. 13b–13f, all cells that exist near to the leading edge split once; in all cases, the first cell to split has $q_{\rm loc} < 0$. In Fig. 13, the positions marked by "a" and "b" correspond to the appearance of new cells. Once more, as A increases, the cell-splitting positions move closer to the leading edge.

In Fig. 13e, vertical lines are again drawn to count easily the number of cells. The left vertical line has eight cells, while it becomes 16 at the third line and 24 at the fourth line. Although the third line from left has 16 intervals, they are unequal in size, which corresponds to the unequal loops of Figs. 11d–11e.

5.3 1:4 Superharmonic Resonance

In this section, we present the nonlinear evolution of the flow on taking the value of forcing frequency to be close

to $\lambda = 0.1$, a quarter of the favoured frequency. These results are shown in Figs. 14–18.

Figure 14 shows the waveform development when $\lambda = 0.09$ and $A = 2 \times 10^{-1}$. Figure 14 shows clearly that there are now four different regions present. The first region is where $\xi \in (70, 132)$, wherein the waves oscillate with the forcing frequency $\lambda = 0.09$. At the end of this region, there is the first transition and two unequal waves appear within each forcing period. Thus, the second region is $\xi \in (132, 257)$. Here the waves constituting each pair are close to one another with a relatively undisturbed region between each pair. It is within these quiescent regions that a new wave develops to give three waves per period in $\xi \in (257, 300)$, and subsequently, a second wave is generated to give four waves per period for $\xi > 300$. At $\xi = 500$, each wave appears to be identical to all other waves and are very similar to those generated by a $\lambda = 0.36$ thermal forcing.

Figure 15 shows the limit cycles of the phase trajectories of the surface rate of heat transfer at various different

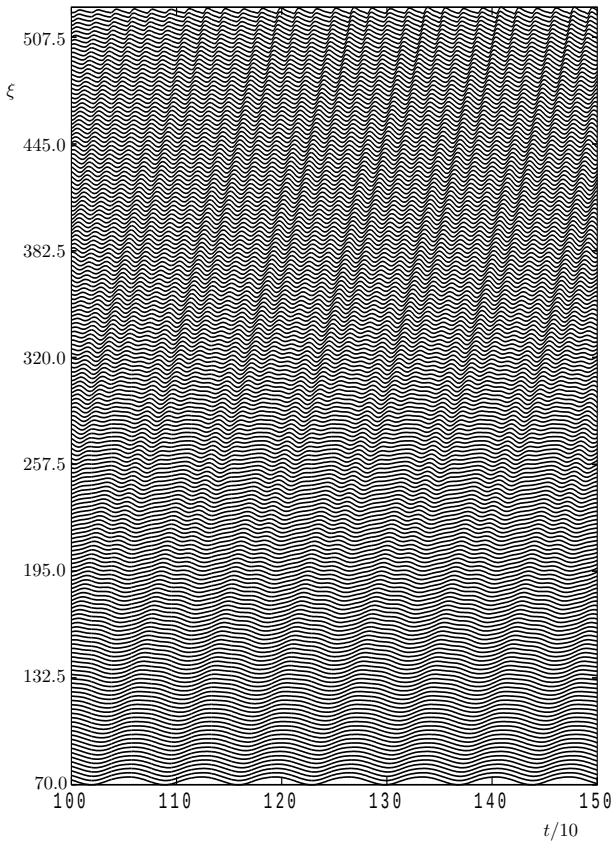

FIG. 14: Waveforms showing the 1:4 superharmonic resonance in the case when $\lambda = 0.09$ and $A = 2 \times 10^{-1}$.

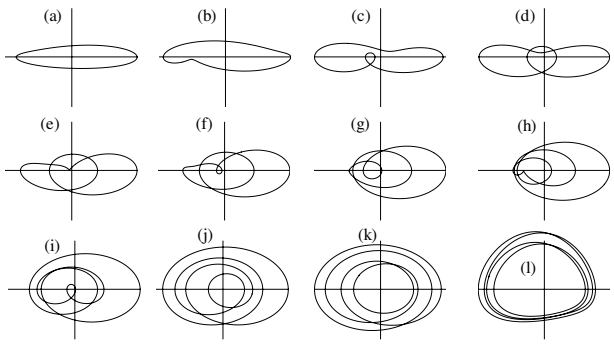

FIG. 15: Limit cycles of the phase trajectories of $q_{\rm loc}$ for $\lambda = 0.09$ and $A = 2 \times 10^{-1}$: (a) $\xi = 50$, (b) $\xi = 125$, (c) $\xi = 175$, (d) $\xi = 200$, (e) $\xi = 225$, (f) $\xi = 238$, (g) $\xi = 250$, (h) $\xi = 263$, (i) $\xi = 288$, (j) $\xi = 313$, (k) $\xi = 338$, and (l) $\xi = 450$. The horizontal coordinate is $q_{\rm loc}$, while the vertical coordinate is $\partial q_{\rm loc}/\partial t$.

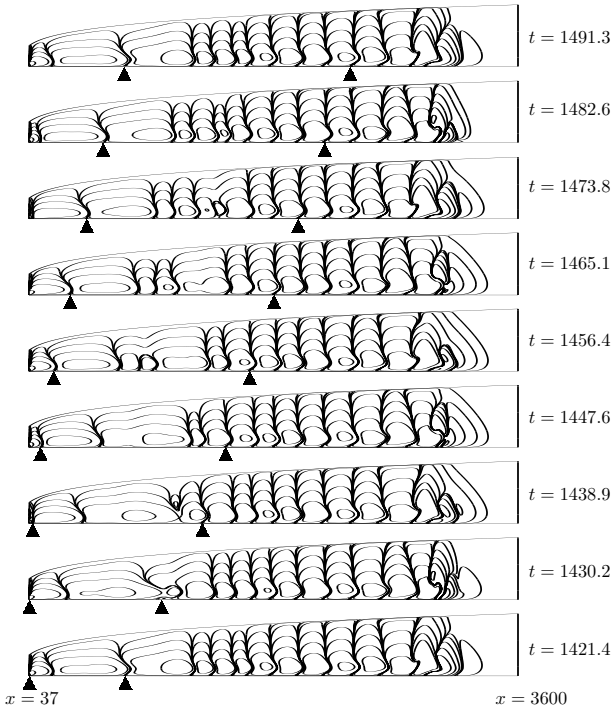

FIG. 16: Contours of $\hat{\theta}$ at eight equally spaced intervals in a forcing period for $\lambda = 0.09$ and $A = 2 \times 10^{-1}$. Corresponding contour levels are plotted for $\hat{\theta} = \pm 5(10^{-1}, 10^{-2}, 10^{-3}, 10^{-4}, 10^{-5}, 10^{-6})$. The black triangles mark a complete cell pair at $t = 1421.4$, which becomes four pairs at time $t = 1491.3$.

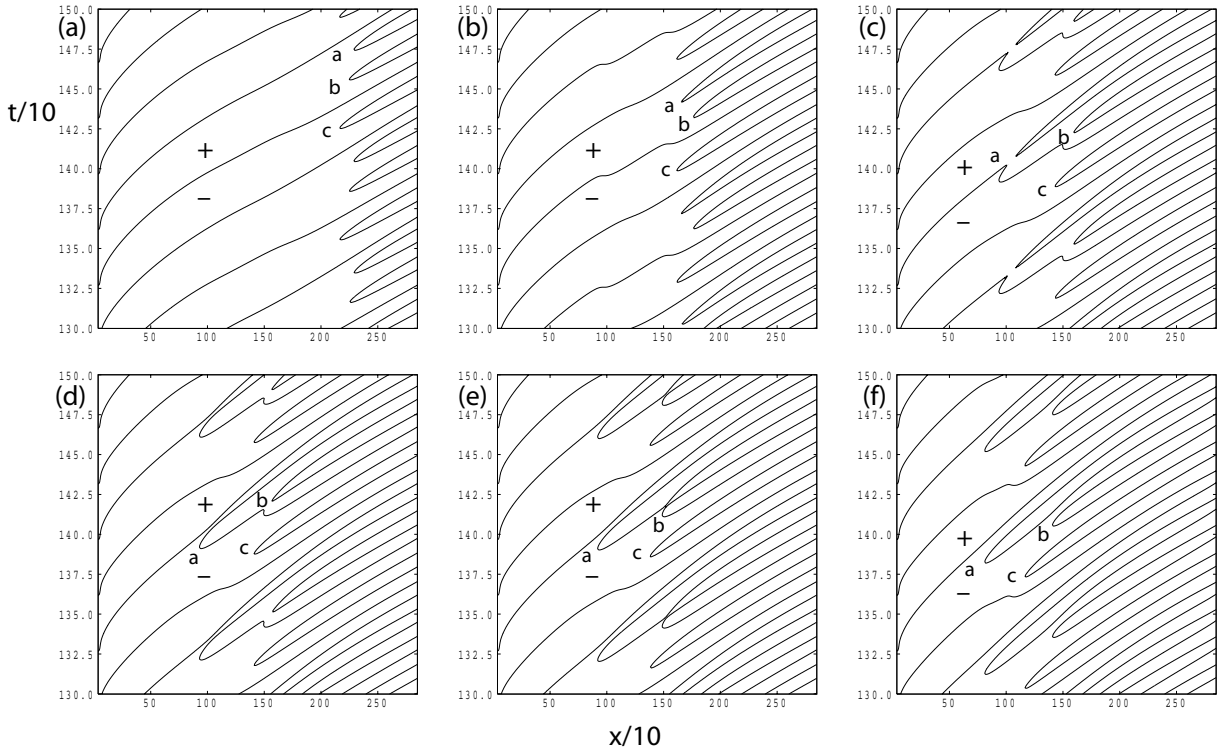

FIG. 17: Zero contours of $q_{\rm loc}$ over the last few periods in time for $\lambda = 0.09$, where (a) $A = 5 \times 10^{-2}$, (b) $A = 10 \times 10^{-2}$, (c) $A = 13 \times 10^{-2}$, (d) $A = 13.4 \times 10^{-2}$, (e) $A = 14 \times 10^{-2}$, and (f) $A = 20 \times 10^{-2}$.

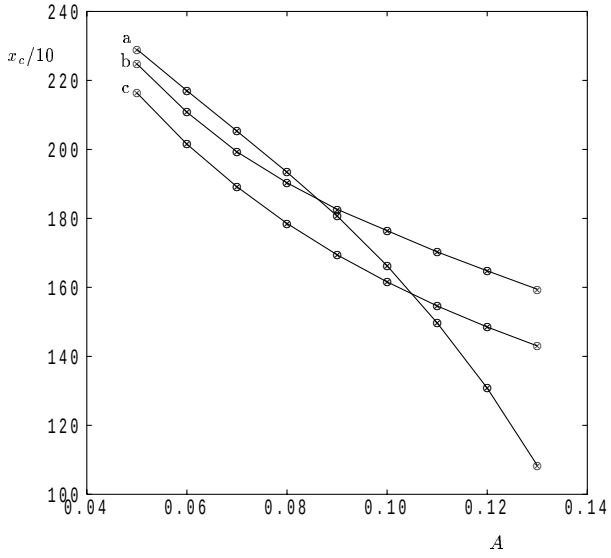

FIG. 18: Variation with A of the location of the turning points of the heat transfer for $\lambda = 0.09$. Three different curves are marked by "a", "b", and "c"denote the positions of the three different turning points in Fig. 17.

positions along the surface. Like the previous superharmonic cases, Fig. 15a shows an almost elliptic shape, indicating that waves are of small amplitude near the leading edge. Generally, the development of the superharmonic resonance sequence is such that extra single loops are added in turn to the phase trajectories. We note that Fig. 15l, which represents the completion of the superharmonic resonance, is just within the nonlinear regime, as may be seen by the non elliptical shape of the trajectories.

Figure 16 shows the corresponding set of disturbance isotherms over eight equally spaced intervals in one forcing period. As t increases, the leading cell elongates compared to the trailing cell and, finally, it splits into seven by a complicated sequence of cell generation.

Contours of $q_{\rm loc} = 0$ shown in Fig. 17 also represent the splitting of cells. The positions at which new cells appear are marked by "a", "b", and "c". In Fig. 17, we see a complicated variation in the way the superharmonic resonance takes place as A increases. In Fig. 17a a region of positive heat transfer, denoted by the plus sign, generates two negative regions, "a"and "b"(so that one cell is trans-

formed into five), while a negative region, denoted by the minus sign, generates one positive region "c"(so one that cell becomes three). Because the positions marked by "a", "b", and "c"are at roughly the same value of x, this means that we have a very sudden change at $x \simeq 2200$ from, say, one pair of cells to four pairs.

Similar comments may be made about Fig. 17b, which corresponds to a larger forcing amplitude. However, the cell marked a now appears before that marked "b". As A increases further, cell splitting occurs much closer to the leading edge and the manner in which the 1:4 resonance takes place alters markedly. When A is as large as 1.34×10^{-1} (Fig. 17d), the first cell splitting creates a central "positive" cell, which subsequently splits to create a central "negative" cell. At larger amplitudes, three positive cells appear within a negative cell, as displayed in Fig. 16. A detailed indication of how the turning points displayed in Fig. 17 vary with A is shown in Fig. 18. This sequence is also affected by changes in the forcing period.

6. SUBHARMONIC RESONANCES $(\lambda > 0.4)$

In Section 5, we presented a selection of cases displaying superharmonic resonances by considering the forcing frequency to be < 0.4. In this section, we present some cases for which the forcing frequency is > 0.4 for various values of the forcing amplitude. We find that, for a wide range of the forcing frequency [$\lambda \in (0.55, 1.0)$], the developing nonlinear flow causes cell merging, which means that the wave train loses half of its cells and that the local wavenumber halves. Specific examples are given for the frequency $\lambda = 0.8$. This is termed a subharmonic resonance and results are displayed in Figs. 19 and 20.

However, in Fig. 19 we provide an overview of our results for different values of both the forcing amplitude and the forcing frequency. The results are presented in terms of the relative maximum local response, $M(x)$, which is defined as

$$M(x) = M_1(x) - M_1(x_{\min}) \tag{12}$$

where

$$M_1(x) = \log_{10} \left| \max_t q_{\rm loc}(x,t) \right|, \tag{13}$$

and that forms the most positive surface rate of heat transfer over time as a function of x, and the relative minimum local response, $N(x)$ as

$$N(x) = N_1(x) - N_1(x_{\min}) \tag{14}$$

where

$$N_1(x) = \log_{10} \left| \min_t q_{\rm loc} \right|, \tag{15}$$

is the magnitude of the most negative surface rate of heat transfer over time. We note that these quantities have been maximized or minimized after the decay of transients as done in Paul et al. (2008).

The value $M_1(x)$ is the logarithm of the maximum temperature gradient at the surface over time once the disturbance has settled into a time-periodic state and is a measure of how strong the waves are. The quantity $M(x)$ measures this strength relative to that at $x = x_{\min}$. Thus, the computed curves for $M(x)$ should be identical when A is sufficiently small and nonlinear effects are negligible. Indeed, within this regime the values of $M(x)$ and $N(x)$ are also identical. However, once A is sufficiently large that the flow becomes nonlinear, then not only does $M(x)$ depend on the value of A, but $M(x)$ and $N(x)$ are no longer equal.

In Fig. 19, each solid curve corresponds to values of $M(x)$ while the dashed curve corresponds to values of $N(x)$. We have plotted four pairs of curves each for different values of A that are marked by a, b, c, and d. Fig. 19a, which corresponds to $\lambda = 0.55$, shows that there is no difference between the values of $M(x)$ and $N(x)$, and they are also independent of A. Thus, the development of the waves follows the linearized theory of Paul et al. (2008).

For $\lambda = 0.6$ and 0.65, the situation is almost exactly the same, although the curves for the largest amplitude, $A = 10^{-2}$, are beginning to deviate from those of smaller amplitudes. When λ is as large as 0.8 and 1.0, the curves for the different amplitudes are very distinct and the shapes of the curves could be interpreted in a variety of ways, including the possibility of mean flow saturation effects. However, linear theory leads us to expect that all the curves for $\lambda = 0.8$ and 1.0 should decay, but for each case three of them do not. Therefore, we have investigated this more closely in Fig. 20, which displays isotherms over two forcing periods for $\lambda = 0.8$ and $A = 10^{-2}$. It is essential to note that nonlinear effects are sufficiently strong that the mean disturbance temperature field over one forcing period is no longer zero, and therefore, we plot contours of $\hat{\theta} - \hat{\theta}_{\rm mean}$ rather than $\hat{\theta}$ only. We note that $50,000$ time steps are taken to obtain time periodic solutions shown in Fig. 20. The immediate response in the region near to the leading edge consists of traveling waves of the type that is consistent with linearized theory for $\lambda = 0.8$, namely fairly rapid decay. However, much further downstream the cells are more consistent with the $\lambda = 0.4$ case and clearly have a longer wavelength.

Black triangles are used in Fig. 20 to clearly show the resonance between these two states. At $t = 4984.3$, the left and middle triangles delimit four cells over two com-

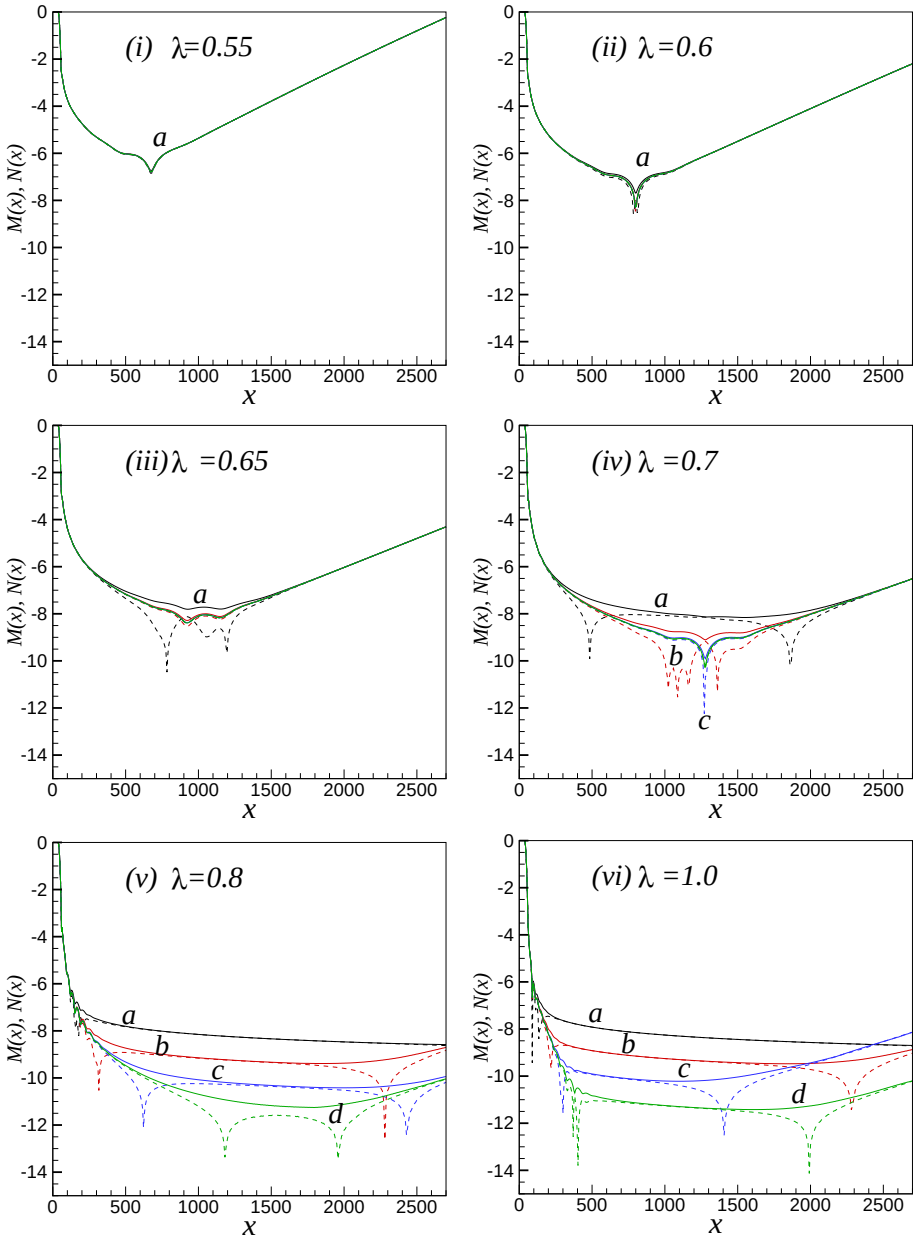

FIG. 19: Curves representing the growth of instabilities for frequencies of > 0.4. Solid lines correspond to $M(x)$, and dashed lines to $N(x)$. Here (a) $A = 10^{-2}$, (b) $A = 10^{-3}$, (c) $A = 10^{-4}$, and (d) $A = 10^{-5}$.

plete forcing periods. As time increases to $t = 5000$, these four cells transform into what is effectively two cells by a process of cell merging, the mechanism for which may be seen by the evolution of the shaded regions with time. Therefore, we what we have is called a subharmonic resonance, where the local spatial wavenumber becomes half of its original value. Similar resonances take place for other disturbance amplitudes, but they take place increasingly far from the leading edge as the amplitude decreases.

Finally, it is worth contemplating the mechanism behind the subharmonic resonance, for it is not as straightforward as the superharmonic resonance, where a straightforward self-interaction mechanism may be in-

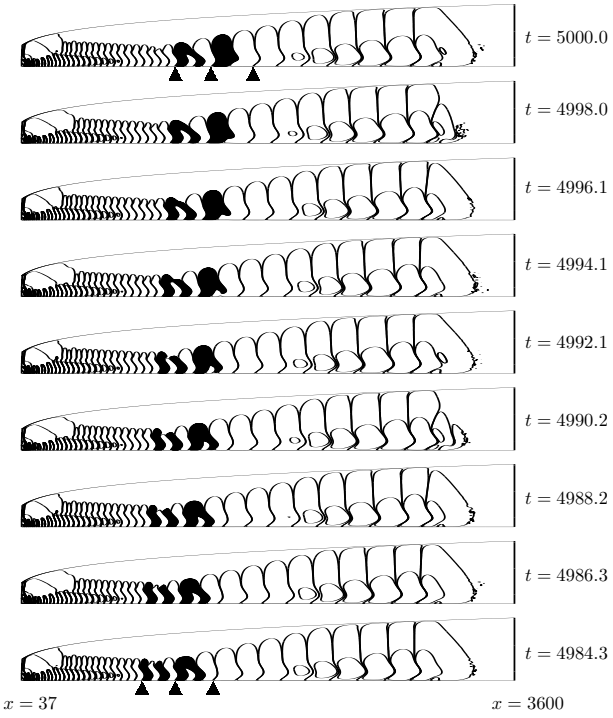

FIG. 20: Contours of $\hat{\theta} - \hat{\theta}_{\rm mean}$ at eight equally-spaced intervals in last two forcing periods. Here $\lambda = 0.8$ and the maximum amplitude is at $A = 10^{-2}$. The corresponding contour levels are at $\pm 6.5(10^{-3}, 10^{-4}, 10^{-5}, 10^{-6}, 10^{-7})$.

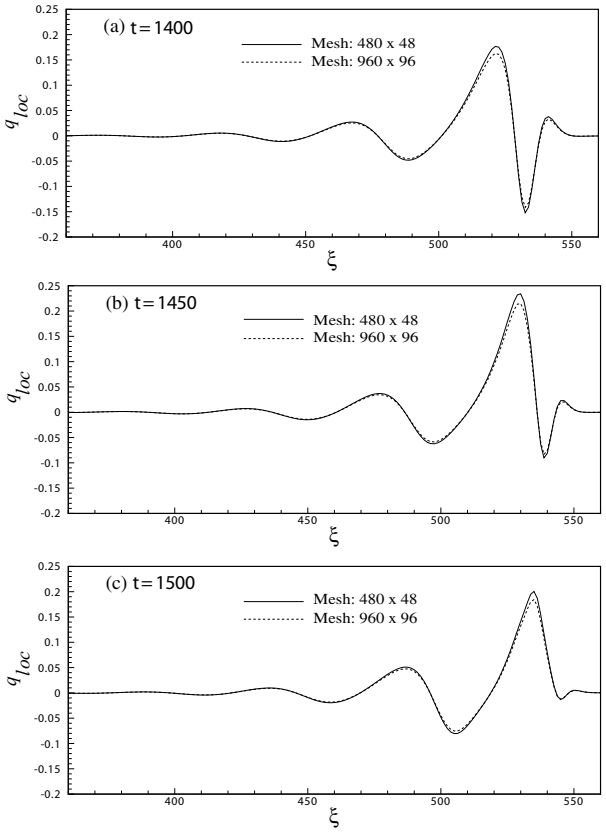

FIG. 21: Mesh independence test showing $q_{\rm loc}$ at three different times for $\lambda = 0.4$ and $A = 2 \times 10^{-5}$.

voked. Subharmonic resonances have also been obtained in vortex convection in porous media [see the review by Rees (2003)], where a nonlinear vortex system of one spanwise wavenumber undergoes a smooth transformation to a system with half the wavenumber. In that convecting system, which is parabolic in space, rather than time, the subharmonic has to be seeded as a small-amplitude disturbance, one that is very much smaller than that which induces the primary vortex system (fundamental). The usual scenario is that the primary vortex system at first grows in strength with distance from the leading edge while the subharmonic disturbance decays. The primary vortex eventually saturates and begins to decay, but the subharmonic then begins to grow. The transition between the primary vortex system being dominant and the subharmonic being dominant is smooth, but quite rapid. All these factors are present for the boundary layer considered here except for the fact that the subharmonic has not been introduced artificially. In an earlier review, Rees (1998), argued that linearized systems such as those considered in Paul et al. (2008), and that are elliptic, may be treated as a partial differential eigenvalue problem whose eigenvalues are complex growth rates and whose eigensolutions are mode shapes. In the present problem, nonlinearities are present even if they are small and the nonlinear interactions between the evolving solution and itself are very likely to contain nonzero components of all the eigensolutions of the linearized form of Eqs. (1)–(3), including one corresponding or closely corresponding to a subharmonic. Nonlinear interactions will then guarantee that the solution with the same frequency as the disturbance frequency will dominate near the leading edge, but a subharmonic that is close to the overall favored frequency will dominate further downstream.

7. CONCLUSIONS

We have studied some aspects of the behaviour of nonlinear waves within the free convective flow from a verti-

cal heated flat plate. A time-periodic thermal disturbance was introduced near the leading edge to generate waves and to find the nonlinear response of the boundary layer. We have found that the nonlinearity has a strong effect on the evolution of waves in the boundary layer, and the waveforms that are realized depend strongly on the forcing frequency and disturbance amplitude.

When the forcing frequency is close to 0.4, which is the linearly most amplified frequency found in Paul et al. (2008) and corresponds to the greatest spatial growth, the resulting flow retains the same frequency [see Fig. 5 of Paul et al. (2008)]. We found that it was difficult to obtain numerical solutions when the disturbance amplitude was larger than approximately 2×10^{-5} due to the inability to resolve the evolving detailed structures with the chosen grid. However, when λ is sufficiently far below 0.4, different types of superharmonic resonance take place. These are characterized by cell splitting in order that the flow resembles closely that corresponding to the favored frequency. The nonlinear interaction of the wave train with itself generates new waves with double, triple, or quadruple the local spatial wavenumber, depending on the precise value of the disturbance frequency and its proximity to an integer submultiple of 0.4.

For frequencies that are > 0.4, we have found that cell merging can take place that halves the wavenumber. We have attempted to explain this mechanism in terms of eigensolutions of the linearized elliptic system. Such resonances are quite well known for systems of vortices where one wavenumber dominates at stations relatively close to the leading edge, but which transform smoothly, if rapidly, to a new system with half the wavenumber [see Chen et al. (1991) and Zuercher et al. (1998), but these are rare for two-dimensional wave instabilities].

To our knowledge, the only experimental study of a vertical boundary layer that concentrates on nonlinear effects is the paper by Szewczyk (1962). In this work, the nonlinear two-dimensional wave train was destabilised by a streamwise vortex system consisting of pairs of vortices, one of which is fairly close to the heated surface while the other is further away. At present, we are unaware whether such a vortex system could be induced in the presence of unsteady thermal disturbances of the type used here, or whether they are a natural consequence of destabilization in a fairly quiescent environment or a product of the dye-injection technique used by that author. But it is clear that a three-dimensional study is required to determine whether the two-dimensional nonlinear phenomena presented here are robust.

ACKNOWLEDGMENTS

The first author acknowledges the receipt of an Overseas Research Studentship (ORS) and thanks the University of Bath for postgraduate funding.

REFERENCES

Arakawa, A., Computational design of long-term numerical integration of the equations of fluid motion: I. Two dimensional incompressible flow, *J. Comput. Phys.*, vol. **1**, pp. 119–143, 1966.

Armfield, S. W. and Patterson, J. C., Direct simulations of wave interactions in unsteady natural convection in a cavity, *J. Fluid Mech.*, vol. 34, pp. 929–940, 1991.

Briggs, W., A Multigrid Tutorial, Lancaster Press, Philadelphia, 1987.

Brooker, A. M. H., Patterson, J. C., and Armfield, S. W., Non-parallel linear stability analysis of the vertical boundary layer in a differentially heated cavity, *J. Fluid Mech.*, vol. **352**, pp. 265–281, 1997.

Chen, C. C., Labhabi, A., Chang, H. C., and Kelly, R. E., Spanwise pairing of finite-amplitude longitudinal vortex rolls in inclined free-convection boundary layers, *J. Fluid Mech.*, vol. **231**, pp. 72–111, 1991.

Fasel, H. and Konzelmann, U., Non-parallel stability of a flat-plate boundary layer using the complete navier-stokes equations, *J. Fluid Mech.*, vol. **221**, pp. 331–347, 1990.

Herwig, H. and You, X., Thermal receptivity of unstable laminar flow with heat transfer, *Int. J. Heat Mass Transfer*, vol. **17**, pp. 4095–4103, 1997.

Janssen, R. and Armfield, S., Stability properties of the vertical boundary layers in differentially heated cavities, *Int. J. Heat Fluid Flow*, vol. **17**, pp. 547–556, 1996.

Kloker, M., Konzelmann, U., and Fasel, H., Outflow boundary conditions for spatial Navier-Stokes simulations of transitional boundary layers, *AIAA J.*, vol. **31**, pp. 620–628, 1993.

Paul, M. C. and Rees, D. A. S., Numerical investigation of the linear stability of a free convection boundary layer flow using a thermal disturbance with a slowly increasing frequency, *ASME J. Heat Transfer*, vol. **130**, p. 122501, 2008.

Paul, M. C., Rees, D. A. S., and Wilson, M., Thermal receptivity of free convective flow from a heated vertical surface: Linear waves, *Int. J. Therm. Sci.*, vol. **47**, pp. 1382–1392, 2008.

Rees, D. A. S., Thermal boundary-layer instabilities in porous media: A critical review, *Transport Phenomena Porous Media*, Ingham, D. B. and Pop, I. (eds), Pergamon, Oxford, 1998.

Rees, D. A. S., Nonlinear vortex development in free convective

boundary layers in porous media, NATO ASI Proc., Neptun, Romania, pp. 449–458, June 9–20, 2003.

Roache, P. J., *Computational Fluid Dynamics*, Hermosa, Albuquerque, 1972.

Szewczyk, A. A., Stability and transition of the free–convection layer along a flat plate, *Int. J. Heat Mass Transf.*, vol. **5**, pp. 903–914, 1962.

Zuercher, E. J., Jacobs, J. W., and Chen, C. F., Experimental study of the stability of boundary-layer flow along a heated, inclined plate, *J. Fluid Mech.*, vol. **367**, pp. 1–25, 1998.

APPENDIX

In Fig. 21, one set of results for the mesh-independence test are presented. Three different instantaneous profiles of q_{loc} for $\lambda = 0.4$ and $A = 2 \times 10^{-5}$ are presented. The agreement found between them is very good and clearly indicate that the 480×48 used here yields a sufficiently well-resolved and accurate solution. The linear stability results contained in Paul and Rees (2008) also showed a similar level of agreement for the mesh-independence tests using the same grids.